



A jigsaw-structured artificial solid electrolyte interphase for high-voltage lithium metal batteries

Luyi Chen¹, Jiawei Lai¹, Zhongliang Li¹, Hanqin Zou¹, Jianghong Yang¹, Kui Ding¹, Yue-Peng Cai¹  [✉] & Qifeng Zheng¹  [✉]

The practical application of lithium-metal batteries is hindered by insufficient lithium Coulombic efficiency and uncontrolled dendrite growth, bringing a challenge concerning how to create robust solid electrolyte interphases (SEIs) that can regulate Li⁺ transport and protect reactive lithium-metal. Here, we present the rational construction of a multi-component jigsaw-like artificial SEI by the integration of fluorine-containing silane and polyether-containing silane. The fluorine-donating group prevents the parasitic reaction and yields a dense structure for homogeneous lithium deposition. Additionally, the lithophilicity of ethylene glycol backbone facilitates the rapid transport of Li⁺ and the cross-linked network increases mechanical robustness of the SEI. With this artificial SEI, we show highly reversible lithium plating and stripping cycling for more than 500 hours. Moreover, we also demonstrate stable operation of high-voltage LiNi_{0.8}Co_{0.1}Mn_{0.1}O₂ cathode in both coin and pouch cells under high loading, limiting excess lithium, and lean electrolyte conditions, holding great prospects for the practical application of high-voltage lithium-metal batteries.

¹School of Chemistry, Guangzhou Key Laboratory of Materials for Energy Conversion and Storage, South China Normal University, 55 West Zhongsan Rd., Guangzhou 510006, China. ✉email: caiy@scnu.edu.cn; qifeng.zheng@m.scnu.edu.cn

Lithium-ion batteries (LIBs) have witnessed numerous developments as the main energy storage device for portable electronics and recently as the dominated assignment for electric vehicles, since their commercialization in 1991^{1,2}. At present, the inherent limitation of energy density for state-of-the-art LIBs (less than 250 Wh kg⁻¹) cannot meet the growing demands from portable electronics, electric vehicles, and grid-scale energy storage. In view of this point, lithium-metal anode (LMA) is the most promising one for replacing the commercial graphite anode of LIBs, thanks to its highest theoretical capacity of 3860 mAh g⁻¹ and lowest electrochemical potential of -3.04 V (*v.s.* standard hydrogen electrode) among all alternative anodes³. Coupling with state-of-the-art high-voltage high-capacity lithium transition metal oxide cathodes (e.g., LiNi_{0.8}Mn_{0.1}Co_{0.1}O₂), the specific energy density of the lithium-metal batteries (LMBs) can reach 450–500 Wh kg⁻¹, which is almost twice that of commercial LIBs^{4,5}. Furthermore, the utilization of Li-metal as anode will allow for the adaption of Li-free cathodes, such as sulfur and air, the specific energy density of the corresponding lithium–sulfur and lithium–air batteries can further boost up to about 650 and 950 Wh kg⁻¹, respectively^{4–6}.

However, the practical application of LMA has been severely hindered by its ultrahigh reactivity with organic electrolytes, leading to continuous parasitic reaction until the Li-metal surface is passivated by a solid electrolyte interphase (SEI) layer. Unfortunately, this in-situ formed SEI cannot withstand infinite volume change during Li plating/stripping process, which give rise to continuous SEI cracking and reformation, consuming both LMA and electrolyte as well as causing low Coulombic efficiency (CE). Even worse, uneven Li deposition is promoted at the cracks of SEI layer, which leads to the growth of deleterious Li dendrites and further results in the formation of dead Li^{7–12}, resulting in rapid battery failure and severe safety hazards.

Recently, growing research efforts have been devoted to developing better LMBs with a fundamental understanding of Li-metal chemistry. Obviously, building a robust SEI on the surface of LMA to circumvent dendrite growth and parasitic reaction is the decisive factor for the practical realization of long-lifespan and safe LMBs^{13–16}. To strengthen the Li-metal/electrolyte interphase, some electrolyte formulations containing various fluorinated solvents and functional additives, *i.e.*, fluoroethylene carbonate¹⁷ and hydrofluoroethers^{18–23}, have been developed to optimize the composition and structure of the native SEI, which has suppressed Li dendrite growth and Li pulverization to an extent, yet its effectiveness is brutally diminished at high current densities. Therefore, alternative artificial SEIs that can stable LMAs have been proposed to replace native SEIs.

For a promising artificial SEI, the following several key requirements must be met simultaneously: (1) high Li⁺ conductivity for rapid Li⁺ transport, (2) excellent mechanical robustness to suppress Li dendrite propagation, (3) high flexibility for good interfacial contact with LMAs, and (4) good compatibility with carbonate-based electrolytes for high-voltage operation. To date, various artificial SEI layers have been constructed to protect LMAs, mainly including inorganic materials and organic polymers. Inorganic materials (e.g., LiF, Li₃PO₄, and Al₂O₃) generally possess high Li⁺ conductivity and excellent mechanical robustness, while suffer from fragility and poor interfacial contact with LMAs. Comparing to inorganic artificial SEIs, organic polymeric SEIs normally feature with high flexibility, good processibility, lightweight, and excellent interfacial contact with LMAs, holding great promise to accommodate LMAs for practical application, yet their inferior Li⁺ conductivity and mechanical robustness remain to be solved.

In accordance with this point, competitive silica-containing organic artificial SEIs, such as silicates^{24,25}, polydimethylsiloxane^{7,26}, silane coupling agent²⁷, and some silica composites^{28–32}, show great

potential for stabilizing LMAs with desirable features, such as good mechanic strength, lithiophilicity, and air tolerance. The high-modulus character of silica-containing artificial SEI can mechanically suppress the Li dendrite growth, the distinct lithiophilicity can regulate Li⁺ flux to smoothen Li⁺ deposition, and air tolerance of LMAs dramatically simplify the fabrication process^{33–38}. Furthermore, the fluoride-rich components have been widely adopted in SEIs to guide the uniform deposition of Li, suppress the growth of Li dendrite, as well as improve Li plating/stripping CE with long cycling performance^{39–43}. Although various artificial SEI strategies have been developed and stable operation of LMAs in ether-based electrolytes has been largely progressed, the ether-based electrolytes are anodically unstable towards the emerging high-voltage cathodes. LMAs with excellent stability in highly oxidative stable, but highly corrosive carbonate-based electrolytes have rarely been reported. Therefore, it would be highly desirable, yet remains a critical challenge, to design an organic artificial SEI layer that possesses high flexibility, excellent mechanical robustness, high Li⁺ conductivity, and especially good compatibility with carbonate-based electrolytes to enable the stable operation of high-voltage LMBs.

Herein, a multi-component jigsaw-like artificial SEI was rationally proposed to realize the stable operation of high-voltage LMBs in commercial carbonate-based electrolyte. By immersing commercial Li foil in a mixture solution of fluorine-containing silane (triethoxy(3,3,3-trifluoropropyl)silane, denoted as F-Si) and polyether-containing silane (bis[(3-methyldimethoxysilyl)propyl]polypropylene oxide, denoted as O-Si), the O-Si molecules were first covalently grafted to Li-metal surface and then copolymerized with F-Si molecules to form a thin and dense multi-component jigsaw-like artificial SEI. As illustrated in Fig. 1, the fluorine-donating group (*i.e.*, -CF₃) is prone to yield a dense structure for uniform Li plating/stripping, as well as being able to suppress dead Li formation and prevent electrolyte decomposition. Furthermore, the ethylene glycol backbone could endow the SEI layer with distinctive lithiophilicity that is favorable for fast Li⁺ transport. Moreover, silicon alkoxy groups (Si-O-C₂H₅ and Si-O-CH₃) from two different silanes could be well connected with each other through polycondensation to form robust cross-linking network, endowing the SEI layer with excellent mechanical strength. Owing to these superiorities, this jigsaw-like SEI protected LMA demonstrates uniform Li plating/stripping without the formation of Li dendrites over 500 h in commercial carbonate-based electrolyte. With this jigsaw-like artificial SEI constructed on LMA, the stable operation of high-voltage Li||LiNi_{0.8}Co_{0.1}Mn_{0.1}O₂ (NCM811) battery is realized even under high cathode mass loading (18 mg cm⁻²), thin Li anode (50 μm), and lean-electrolyte condition (5 μL mg⁻¹), demonstrating great potential for its practical application in LMBs.

Results and discussion

Design and construction of jigsaw-like artificial SEI. As can be seen in Supplementary Fig. 1, without the protection of artificial SEI, the Li dendrites tend to grow on the surface of pristine LMA during repeated plating/stripping cycles, especially in commercial carbonate-based electrolytes, which leads to battery failure and potential safety hazards. To solve this challenge, the inexpensive saline coupling agents have recently been proposed to stabilize the Li-metal/electrolyte interfaces by forming Li-O-Si covalent bonds with Li-metal, nevertheless, these single-component artificial SEIs cannot meet all the desirable properties discussed above, including high Li⁺ conductivity, excellent mechanical robustness, high flexibility, and good compatibility with carbonate-based electrolytes.

Therefore, a multi-component jigsaw-like artificial SEI was rationally designed by reacting the Li-metal with two types

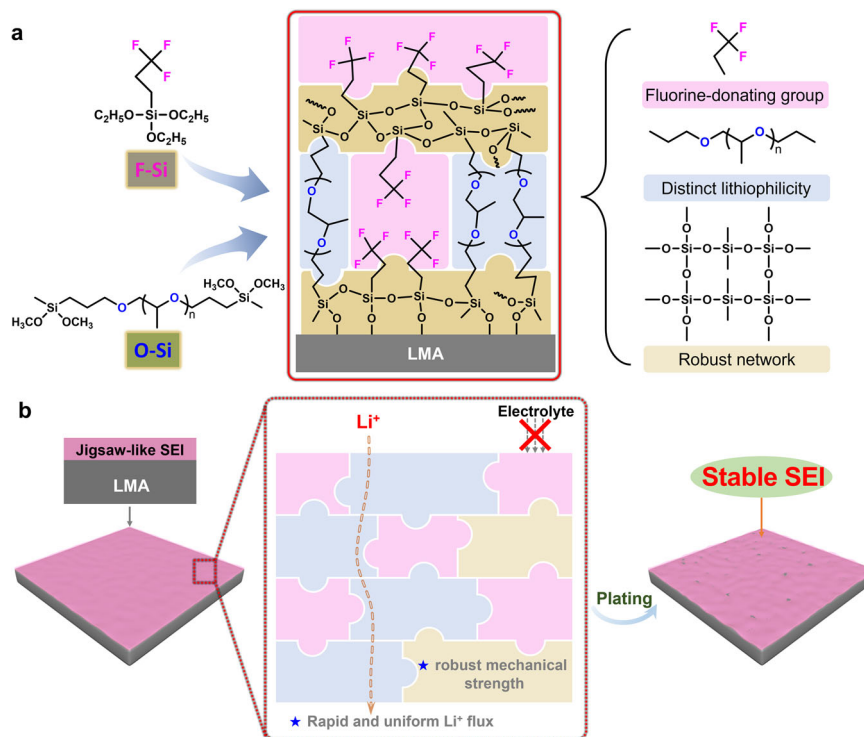


Fig. 1 Schematic diagram of the jigsaw-like artificial SEI. **a** Schematic illustration of designing multi-component jigsaw-like artificial SEI, where the fluorine-donating group (i.e., $-\text{CF}_3$) could yield a dense structure to prevent the formation of Li dendrites and the decomposition of electrolytes, the ethylene glycol backbone is favorable for rapid Li^+ transport, the robust cross-linking network could endow the SEI layer with excellent mechanical strength. **b** Stable Li plating/stripping behavior of LMA with jigsaw-like SEI.

of silanes, including fluorine-containing silane (i.e., F-Si) and polyether-containing silane (i.e., O-Si). The thus-derived artificial SEI is denoted as FO-Si layer, and the thus-derived Li-metal is denoted as FO-Si@Li. As a rationale, the fluorine-donating group (i.e., $-\text{CF}_3$) from F-Si could block the corrosive electrolyte and yield a dense structure that is beneficial to prevent dead Li formation and suppress electrolyte decomposition, ethylene glycol backbone from O-Si was introduced as the Li^+ conductive sites for fast Li^+ transport, and the cross-linking network based on silicon alkoxy groups could endow the feature of viscoelastic with robust mechanical strength.

As shown in Fig. 1a and Supplementary Fig. 2, due to the presence of trace LiOH on the surface of Li-metal (Supplementary Fig. 3), by immersing the Li-metal in F-Si/O-Si/tetrahydrofuran (THF) mixture solution, both F-Si and O-Si could graft spontaneously to the surface of Li-metal based on the chemical reaction of alkoxy groups with LiOH to form Si-O-Li covalent bonds. Furthermore, both F-Si and O-Si could induce condensation reaction with each other to form a robust cross-linking network, which was then assembled into a thin and dense multi-component artificial FO-Si layer. The volume ratio of the F-Si and O-Si in the mixture solution was optimized to be 1:1. For comparison purpose, the single-component artificial SEI was also prepared by treating the Li-metal solely with F-Si or O-Si silane (denoted as F-Si layer or O-Si layer, respectively), of which the corresponding properties were systematically investigated.

According to the X-ray diffraction (XRD) spectra of Li-metal before and after treated with different silanes (i.e., F-Si, O-Si, or F-Si/O-Si), the peak associated with LiOH was disappeared for FO-Si@Li and O-Si@Li, demonstrating the successful bonding reaction of both silanes with Li-metal (Supplementary Fig. 3). While the LiOH peak still presented for F-Si@Li, which may be ascribed to the electron-withdrawing effect of the $-\text{CF}_3$ group that

reduces the reactivity of the F-Si silane. The surface morphology of the FO-Si@Li was observed by scanning electron microscopy (SEM) and shown in Supplementary Fig. 4a, which is flat and smooth. Furthermore, the homogeneous distributions of F, Si, O, and C elements could be observed in the elemental mapping images, suggesting that FO-Si layer covers the Li-metal uniformly with a thickness of ~ 200 nm (Supplementary Fig. 5). As shown in the X-ray photoelectron spectroscopy (XPS) spectra of FO-Si@Li in Supplementary Fig. 4b, a distinct peak of 101.4 eV was observed for Si 2p, which is ascribed to C-Si-O, demonstrating that silanes were grafted on the surface of the Li-metal. Meanwhile, both C-F (687.9 eV) and LiF (684.7 eV) signals were observed, indicating the successful introduction of fluorine-donating groups to the artificial SEI. Moreover, the surface morphologies of the F-Si@Li and O-Si@Li were also observed in Supplementary Figs. 6 and 7.

The time-of-flight secondary-ion mass spectrometry (TOF-SIMS) was conducted to intuitively characterize the chemical components on fresh FO-Si@Li. As shown in the TOF-SIMS depth profiles of selected ion fragments in Fig. 2a, F^- , C_2^- , and CHO_2^- corresponding to organic components that derived from F-Si and O-Si, as well as Si^- , SiO_2^- , and SiCH_3O^- belonging to the inorganic components of silyl group, were detected, demonstrating the multi-component features of this artificial SEI that is enriched of fluorine, oxygen, and silicon. Furthermore, the 3D TOF-SIMS mapping images corresponding to the depth profiles in Fig. 2b also exhibits a uniform distribution of F^- , C_2^- , CHO_2^- , Si^- , SiO_2^- , and SiCH_3O^- fragments throughout the sputtering depth, proving the uniformity of jigsaw-like SEI layer on the surface of Li-metal.

The mechanical property of an artificial SEI is of vital importance to accommodate the immense volume change of LMAs and suppress the growth of Li dendrites. As shown in Supplementary Figs. 8a and 9a, the F-Si layer itself is very brittle and cannot form a free-standing film, while the O-Si layer exhibited superior

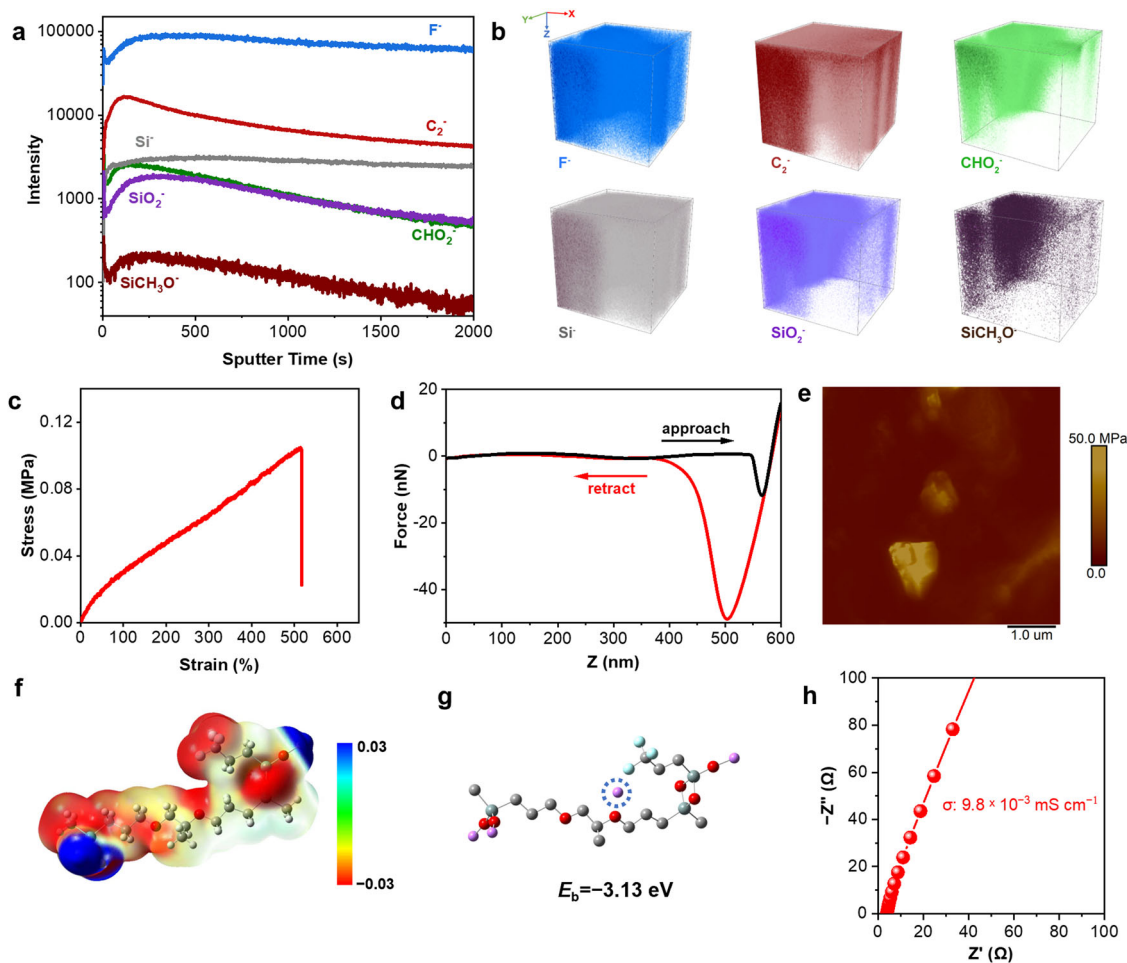


Fig. 2 Characterizations of jigsaw-like artificial FO-Si layer. **a** TOF-SIMS depth profiles of selected secondary-ion fragments on the surface. **b** The 3D view images of the sputtered volume corresponding to the depth profiles. **c** Tensile stress-strain curve. **d** Typical force-displacement curve. **e** AFM Young's modulus mapping. **f** The electrostatic potential. **g** Binding energy with Li^+ . **h** Electrochemical impedance spectrum for ionic conductivity measurement.

elasticity (stretchability of $\sim 380\%$) with a moderate tensile strength of 0.18 MPa. By integrating the F-Si and O-Si silanes, the resulting multi-component jigsaw-like artificial FO-Si layer demonstrated higher mechanical strength of 0.22 MPa without sacrificing the elasticity (stretchability of $\sim 390\%$, Fig. 2c). Atomic force microscopy (AFM) was performed to further analyze the surface layers of F-Si@Li, O-Si@Li, and FO-Si@Li. According to the force-displacement curves and AFM Young's modulus mappings shown in Fig. 2d, e and Supplementary Figs. 8 and 9, the jigsaw-like artificial FO-Si layer showed a perfect balance between elasticity and strength, while F-Si layer is too brittle and O-Si layer is too soft, which agrees well with tensile stress-strain results.

In addition, the electrostatic potential calculations showed that the negative charges were located at both O and F atoms in FO-Si SEI layer (Fig. 2f), which could contribute to the coordination with positive Li^+ . Indeed, according to the density-functional theory calculations (Fig. 2g), the FO-Si jigsaw-like SEI layer showed a more negative binding energy with Li^+ than that of F-Si and O-Si SEI layers (Supplementary Figs. 8 and 9), which would favor the homogeneous deposition of Li. Therefore, the ionic conductivity of SEI layers were further measured, which agrees well with our hypothesis that the FO-Si jigsaw-like SEI layer exhibited the highest ionic conductivity of $9.8 \times 10^{-3} \text{ mS cm}^{-1}$ (Fig. 2h). Moreover, the Li^+ transference number (t_{Li^+}) for the pristine Li-metal was calculated to be 0.16, while the t_{Li^+}

value for FO-Si@Li was increased to 0.63 (Supplementary Figs. 10 and 11), which is beneficial for suppressing the Li^+ concentration gradient at the interface and realizing uniform Li deposition. Therefore, through the rational design of multi-components with robust cross-linking network, the resulting jigsaw-like artificial SEI not only exhibits excellent mechanical robustness for suppressing the growth of Li dendrites, but also has high Li^+ conductivity and high Li^+ transference number for rapid Li^+ transport, holding great promise to implement LMAs in next-generation batteries.

Jigsaw-like SEI stabilized LMAs. First, to verify the chemical stability of jigsaw-like SEI towards corrosive carbonate-based electrolyte, Li||Li symmetric cells fabricated with various Li-metal and commercial electrolyte of 1 M lithium hexafluorophosphate (LiPF_6) in ethylene carbonate (EC): dimethyl carbonate (DMC) by 1:1 volume ratio (denoted as 1 M LiPF_6 in EC/DMC) were analyzed by electrochemical impedance spectroscopy. As shown in Supplementary Fig. 12, the interfacial impedance of the pristine Li||Li cell increases obviously with different standing time, indicating continuous parasitic reaction between pristine Li and electrolyte. With the protection from artificial SEI, all three Li||Li cells exhibit very stable interfacial impedance with the FO-Si@Li cell being the most stable, demonstrating its superior stability as well as the effectiveness in blocking the electrolyte.

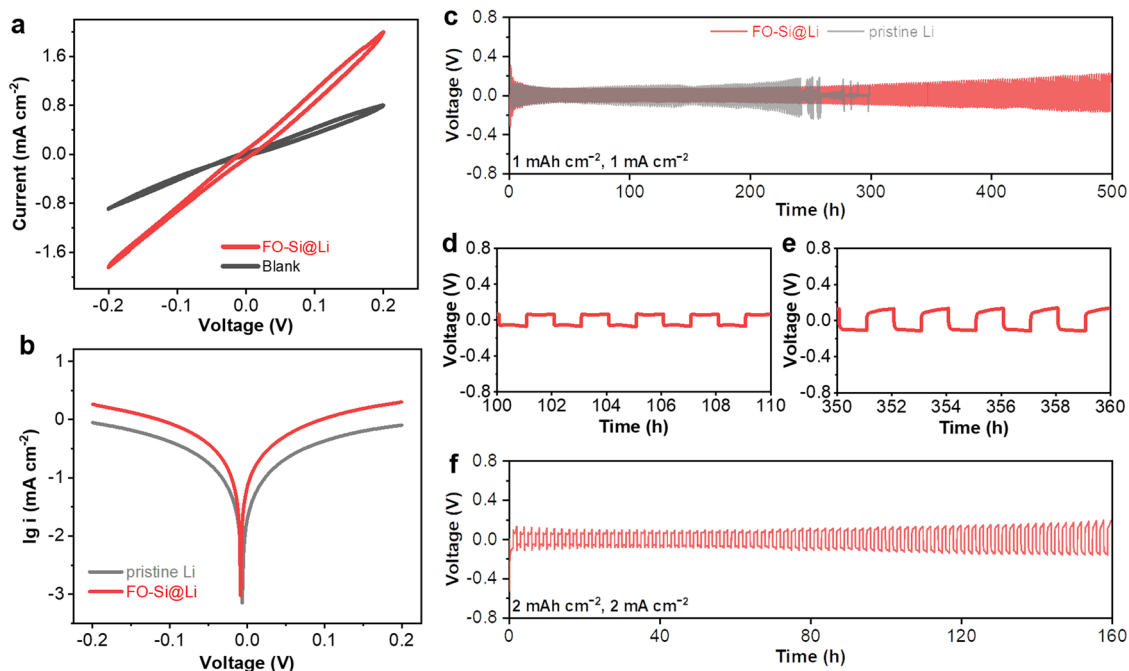


Fig. 3 Electrochemical stability of LMA with jigsaw-like SEI. **a** Cyclic voltammograms and **b** the corresponding Tafel plots of Li||Li symmetric cell measured at a scan rate of 1.0 mV s^{-1} between -0.2 and 0.2 V . **c** Long-term cycling of Li||Li symmetric cells at 1 mA cm^{-2} with a capacity of 1 mAh cm^{-2} . The enlarged voltage profiles of the **d** 100^{th} – 110^{th} and **e** 350^{th} – 360^{th} hours of Li||Li symmetrical cells at 1 mA cm^{-2} with a capacity of 1 mAh cm^{-2} . **f** Long-term cycling of Li||Li symmetric cell using FO-Si@Li at 2 mA cm^{-2} with a capacity of 2 mAh cm^{-2} .

To evaluate the reaction kinetics of LMAs, cyclic voltammetry (CV) measurement was also executed for symmetric cells for the initial five cycles. Both CV curves exhibit typical centrosymmetric loops shown in Fig. 3a, indicating highly reversible electrochemical behavior. Compared with the pristine Li electrode, the FO-Si@Li electrode showed a more pronounced current with two broad peaks at about 0.13 and -0.13 V over the following cycles, confirming the distinct lithophilicity of this jigsaw-like SEI that promote the highly reversible plating/stripping of Li. Furthermore, as shown in Fig. 3b and Supplementary Fig. 13, Tafel curves demonstrated that the FO-Si@Li electrode exhibited higher exchange current density (i.e., 0.270 mA cm^{-2}) than that of pristine Li (i.e., 0.107 mA cm^{-2}), suggesting that the jigsaw-like SEI is featured with fast kinetic that can accelerate Li^+ migration^{31,44}.

Thereafter, the Li||Li symmetric cells assembled with various Li electrodes and commercial carbonate-based electrolyte were subjected to galvanostatic cycling test. As shown in Fig. 3c–e and Supplementary Fig. 14, at a current density of 1 mA cm^{-2} with a constant capacity of 1 mAh cm^{-2} , the cell with a pristine Li electrode experienced a hard short-circuit within only 230 h due to the generation of highly porous and dead Li (Supplementary Fig. 15). In contrast, the cell with a FO-Si@Li electrode displayed very stable Li plating/stripping for over 500 h, which outperforms most of the reported Li electrode in carbonate-based electrolyte (Supplementary Table 1), demonstrating the superiority of this jigsaw-like artificial SEI for favorable dendrite-free Li plating/stripping behavior. Furthermore, the interfacial resistance of the cell using FO-Si@Li electrode decreases gradually during the initial several cycles and then remains stable and small in the subsequent cycling (Supplementary Fig. 16), ascribing to the high Li conductivity and excellent interfacial stability of the multi-component artificial SEI. However, the interfacial resistance of the Li||Li cell using pristine Li electrode starts to increase after 100 cycles, suggesting that the native SEI is vulnerable and cannot sustain the stable operation of LMAs. Meanwhile, the stability of FO-Si@Li electrode after 100 cycles was verified by

SEM and XPS tests in Supplementary Fig. 17. The smooth Li surface from SEM image, homogeneous distributions of F, Si, O, and C shown in the elemental mapping images, and chemical compositions from XPS results, are all consistent with that of FO-Si@Li electrode before cycling, demonstrating the protectiveness of jigsaw-like artificial SEI.

Furthermore, to intuitively show the advantage of this jigsaw-like artificial SEI, the Li deposition behavior was observed by in operando optical microscopy (Fig. 4). At a plating current density of 1 mA cm^{-2} , mossy and dendritic Li started to generate on the pristine Li electrode at 20 min and continuously to grow during the following process. In sharp contrast, a dendrite-free and smooth surface was observed for the FO-Si@Li throughout the plating process, confirming that the jigsaw-like artificial SEI plays an important role in stabilizing the interface as well as inhibiting the growth of dendritic Li.

When the current density was increased to 2 mA cm^{-2} with a capacity of 2 mAh cm^{-2} , the cell with a FO-Si@Li electrode still delivered a decent cycling stability for over 160 h with small and stable voltage polarization (Fig. 3f). It should be noted that there are some previously reported artificial SEIs demonstrated longer Li cycle life even under higher current densities and larger areal capacities^{24,27,44,45}. However, such good performance can only be achieved in Li-metal friendly ether-based electrolytes, their effectiveness would be severely deteriorated in commercial carbonate-based electrolytes. In other words, by using ether-based electrolyte, our jigsaw-like artificial SEI is easily to enable the stable cycling of Li||Li cells for over thousands of cycles (Supplementary Fig. 18). Nevertheless, the application of ether-based electrolytes is severely hindered by its low oxidation potential ($<4 \text{ V}$ vs Li^+/Li), which is incompatible with the emerging high-voltage cathodes, and therefore our study is focused on improving Li-metal compatibility in high-voltage tolerance carbonate-based electrolytes.

Replacing the conventional graphite anode with LMA has been proven to increase the cell energy density by 40–50%⁴⁶. However, this substantial increase in energy density can be achieved only if

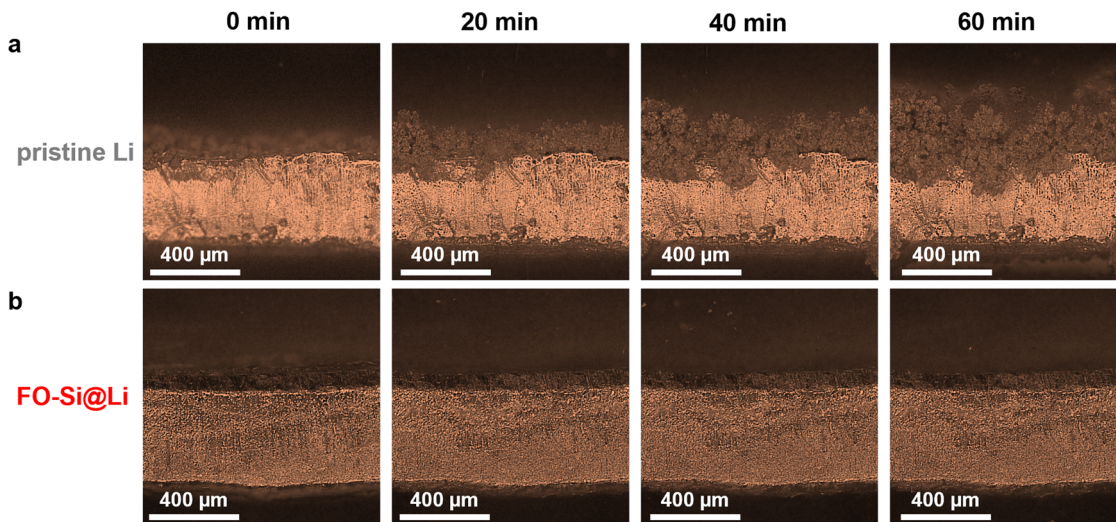


Fig. 4 In operando observation of Li deposition. In operando optical microscopy images of Li deposits on **a** pristine Li and **b** FO-Si@Li upon plating time at a current density of 1 mA cm^{-2} .

limiting excess Li is employed. Therefore, Li||Li symmetric cells with a thin Li of $50 \mu\text{m}$ were also investigated. As shown in Supplementary Figs. 19 and 20, similar to that of thick Li electrode, the thin Li||Li cell with the protection of designed jigsaw-like artificial SEI can still exhibited good cycling stability at both current densities of 1 and 2 mA cm^{-2} , while the thin Li||Li cell with pristine Li electrode cannot operate normally and fails within a few cycles. These results suggested that this multi-component artificial SEI may be able to enable the stable operation of high-voltage LMBs with limiting excess Li (i.e., thin Li).

The superior electrochemical performance of FO-Si@Li electrode could be ascribed to the following integrated merits of multi-component jigsaw-like artificial SEI: (1) the fluorine-donating group effectively prevents the decomposition of electrolytes as well as yields a dense structure for homogeneous Li deposition; (2) distinct lithophilicity of ethylene glycol backbone facilitates the rapid transport of Li^+ across the SEI; (3) robust cross-linking Si-O-Si network well accommodates the immerse volume change of LMA as well as suppresses the growth of Li dendrites.

High-voltage LMBs under high loading, limiting excess Li, and lean-electrolyte conditions. To evaluate the potential application of jigsaw-like SEI in practical high-voltage batteries, the FO-Si@Li anode was paired with a NCM811 cathode, an emerging high-voltage high-capacity cathode for commercialized Li-ion batteries. With a cutoff voltage window of 3.0–4.3 V, as can be seen in the first galvanostatic charge-discharge (GCD) curve at 0.1 C in Fig. 5a, the FO-Si@Li||NCM811 cell exhibited a high initial capacity of 193 mAh g^{-1} with a low charge voltage platform and high CE of 87.4%, which is better than that of pristine Li anode that may be suffered from irreversible reaction between Li-metal and carbonate-based electrolyte (CE of 83.5%). Furthermore, the FO-Si@Li||NCM811 cell delivered an extremely stable cycling with an excellent capacity retention of 80.1% and a high average CE of 99.9% over 500 cycles at 1 C in Fig. 5b. Although the pristine Li||NCM811 cell exhibited a relatively stable cycling during the first 150 cycles, its capacity was severely decayed in the subsequent cycles, which could be ascribed to the continuous parasitic reaction that leads to the consumption of electrolyte and formation of dead Li, resulting in the accumulation of thick and resistive interfacial layer. Moreover, the selected GCD curves during cycling were shown in Fig. 5c, and the

overpotential was reflected by calculating the mid-point voltage gaps (ΔV) from GCD curves shown in Fig. 5d. As can be seen, the FO-Si@Li||NCM811 cell exhibited very small overpotential during cycling, with a small ΔV of about 20 mV even after 500 cycles. While the pristine Li||NCM811 cell showed a severe overpotential increase after 150 cycles and the ΔV exceeded 60 mV after 200 cycles. This is attributed to the stable jigsaw-like SEI that effectively suppresses the parasitic reaction between LMA and electrolyte as well as regulates the uniform Li deposition.

The cycling behaviors at a high rate of 2 C were also investigated and shown in Supplementary Fig. 21. The FO-Si@Li||NCM811 cell can still deliver an extremely stable cycling performance with high CE and low overpotential. Furthermore, as shown in Fig. 5e, the FO-Si@Li||NCM811 cell also showed excellent rate capability, where a high discharge capacity of 140.0 mAh g^{-1} was retained even at a high rate of 5 C, outperforming pristine Li||NCM811. In addition, owing to the high t_{Li^+} and Li^+ conductivity offered by jigsaw-like artificial SEI, low overpotentials at various testing rates were observed for the FO-Si@Li||NCM811 cell with a small ΔV of 220 mV at 5 C (Fig. 5f). In contrast, the ΔV of pristine Li||NCM811 cell reached 376 mV at 5 C.

Additionally, the effectiveness of this jigsaw-like artificial SEI was further verified in a practical Li||NCM811 cell with high cathode mass loading of $\sim 18 \text{ mg cm}^{-2}$ (corresponding to a high areal capacity of $\sim 3.6 \text{ mAh cm}^{-2}$) and lean electrolyte of $5 \mu\text{L mg}^{-1}$. As shown in Fig. 6a, under such harsh test condition, the FO-Si@Li||NCM811 cell can still retain 60% capacity after 100 cycles at 1 C. In sharp contrast, the pristine Li||NCM811 cell can only survive for ~ 30 cycles, which may be ascribed to the fact that massive dead Li tend to form and the electrolyte drying up easily under high loading and lean electrolyte. Furthermore, the FO-Si@Li||NCM811 cell also showed much lower overpotential compared to the pristine Li||NCM811 cell during cycling (Fig. 6b). The surface morphologies of the LMAs in Li||NCM811 cells after cycling were investigated. As show in Fig. 6c, the FO-Si@Li anode after 100 cycles exhibited a smooth and shiny surface, demonstrating that FO-Si jigsaw-like artificial SEI could guide the uniform deposition of Li^+ and suppress the formation of dendritic/dead Li. While pristine LMA showed evident porous and dendritic Li structure, leading to rapid battery failure (Fig. 6d). Moreover, the XPS results of FO-Si@Li anode after 100 cycles in Supplementary Fig. 22 are consistent with fresh FO-Si@Li anode (i.e., before cycling) in Supplementary Fig. 4b,

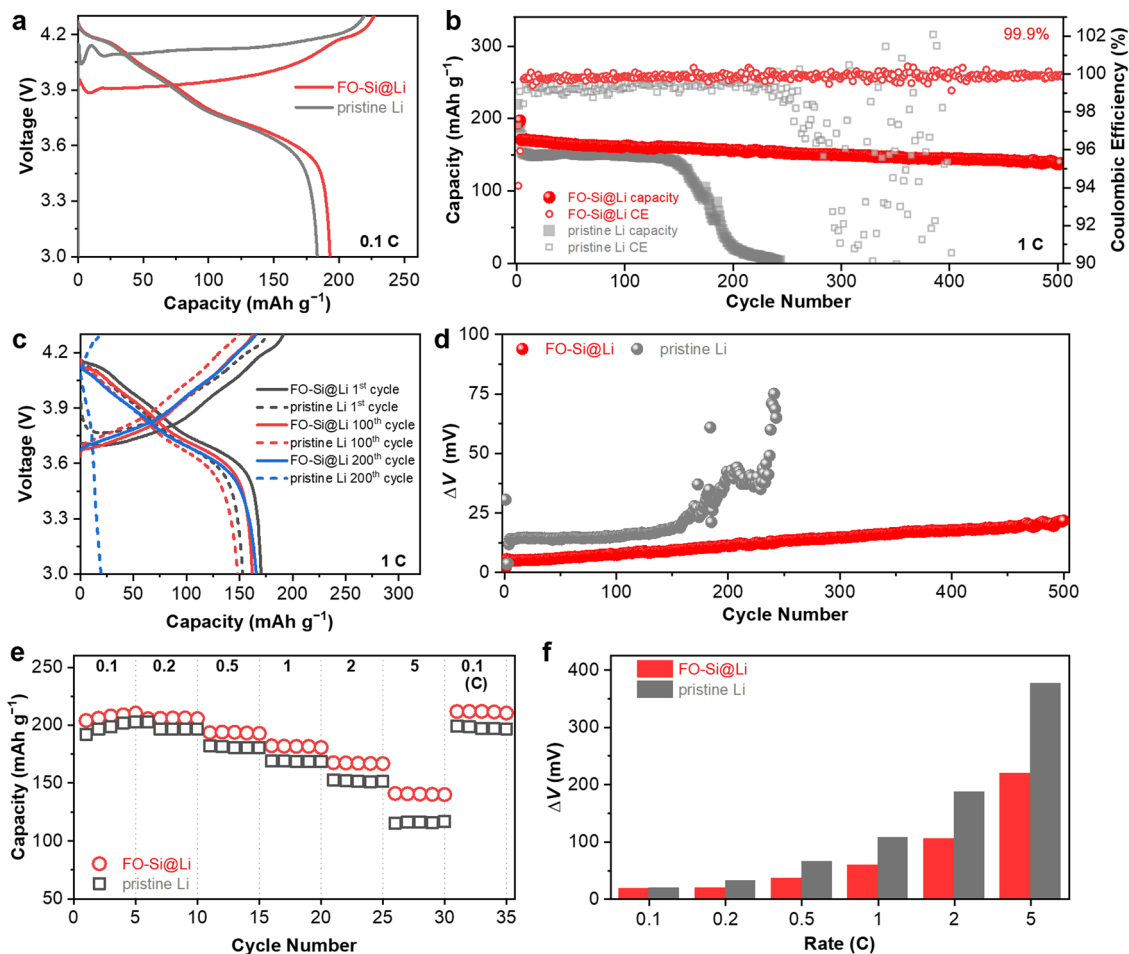


Fig. 5 Electrochemical performance of Li||NCM811 coin cells with a thick Li of 500 μm . **a** The initial GCD curves at 0.1 C. **b** Cyclic performance at 1 C after three formation cycles at 0.1 C. **c** Selected GCD curves at 1 C. **d** Overpotential (ΔV) at different cycles. **e** Rate capability and **f** its corresponding overpotential (ΔV) at various rates.

suggesting the superior stability of FO–Si jigsaw-like artificial SEI in the harsh test, which further demonstrates the effectiveness of constructing this multi-component jigsaw-like SEI to enable practical LMBs under high loading and lean-electrolyte condition.

As previously discussed, limiting excess Li is one of the most prerequisites for realizing practically high-energy LMBs. Therefore, the FO–Si@Li||NCM811 full cell was also assembled based on a thin Li foil of 50 μm . As shown in Fig. 7a, the 50 μm thin FO–Si@Li||NCM811 full cell delivered extremely stable cycling performance with more than 95% capacity retained after 150 cycles at 1 C. Furthermore, the GCD curves do not show an obvious increase in overpotential upon cycling (Fig. 7b), indicating superior interfacial compatibility even with limiting excess Li. While testing at 2 C, the cell could also maintain excellent capacity retention with low overpotential (Supplementary Fig. 23).

To further validate the protection of this artificial SEI modified Li-metal in practical operation, a single-layer pouch cell of Li||NCM811 was assembled with a high mass loading cathode ($\sim 18 \text{ mg cm}^{-2}$) and a FO–Si artificial SEI protected thin Li (50 μm). The electrolyte/cathode ratio was controlled at low value of 5 $\mu\text{L mg}^{-1}$. For the initial three formation cycles at 0.1 C, the pouch cell shows an initial capacity of 204 mAh g^{-1} , with an average discharge voltage of 3.82 V, corresponding to an energy density of 677 Wh kg^{-1} based on the total weight of cathode and anode. Thereafter, the FO–Si@Li||NCM811 pouch cell showed a discharge of 180 mAh g^{-1} at 0.5 C and was held at 171 mAh g^{-1} after 50 cycles with very small overpotentials (Fig. 7c, d). Moreover,

this pouch cell was applied to power electronic devices to for practical validation. As shown in Fig. 7e, f, this pouch cell can light up a red LED for 10 min or power two micromotors for 30 s, indicating the great potential of this jigsaw-like SEI for protecting LMAs to enable the practical application of LMBs.

Conclusion

In conclusion, a multi-component jigsaw-like artificial SEI was rationally designed by taking the synergistic advantages of fluorine-donating silane and ethylene glycol backbone-containing silane as well as their capability to crosslink with each other to form robust cross-linking network. The fluorine-donating group (i.e., $-\text{CF}_3$) could effectively prevent the decomposition of electrolytes as well as yield a dense structure for homogeneous Li deposition. Furthermore, the distinct lithophilicity of ethylene glycol backbone and robust cross-linking network could facilitate the rapid transport of Li^+ and increase the mechanical robustness of the resulting artificial SEI. As a result, the as-constructed jigsaw-like artificial SEI can deliver the stable Li plating/stripping for more than 500 h in corrosive carbonate-based electrolytes. Thanks to its superior compatibility with oxidation-tolerant carbonate electrolyte, this jigsaw-like artificial SEI protected-Li is demonstrated to enable the stable operation of high-voltage NCM811 cathode in both coin and pouch cells even under high cathode loading (18 mg cm^{-2}), limiting excess Li (50 μm), and lean-electrolyte conditions ($5 \mu\text{L mg}^{-1}$). This work demonstrates the effectiveness of designing jigsaw-like SEI from cost-effective

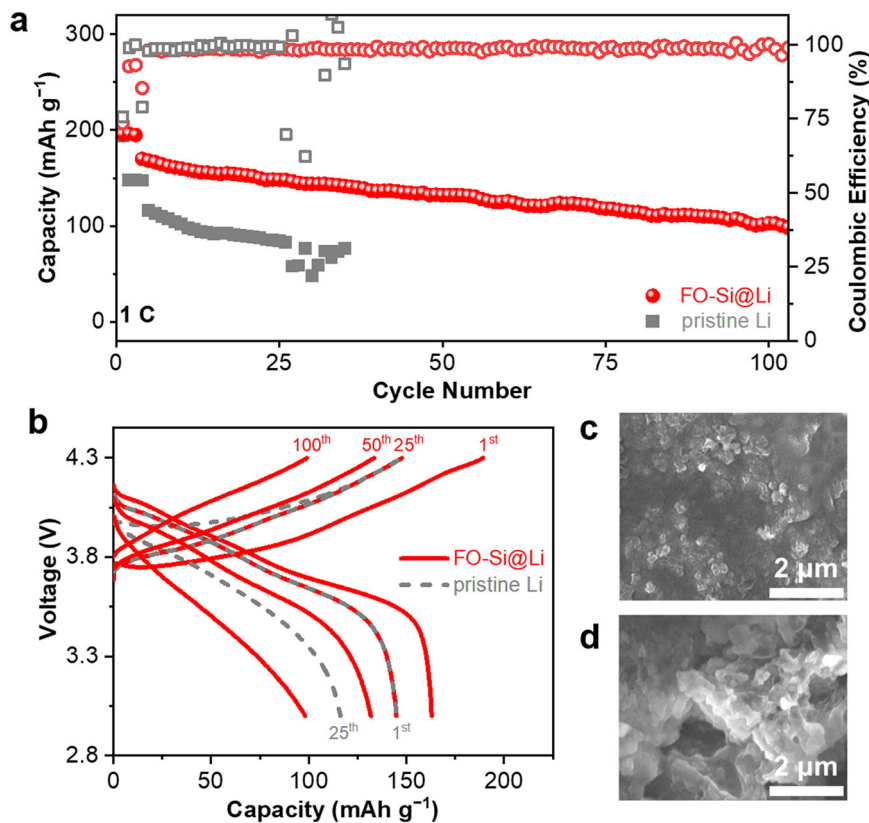


Fig. 6 Electrochemical performance of Li||NCM811 coin cells at high cathode mass loading of 18 mg cm^{-2} and lean-electrolyte of $5 \mu\text{L mg}^{-1}$. **a** Cyclic performance at 1C after three formation cycles at 0.1C. **b** Selected GCD curves at 1C during cycling. **c** SEM images of FO-Si@Li anode after 100 cycles and **(d)** pristine Li anode after 30 cycles.

silanes in stabilizing LMAs, which provides a splendid strategy for the development of other metal anodes such as Na and Zn anodes.

Methods

Chemicals. Triethoxy(3,3,3-trifluoropropyl)silane (F-Si) and bis[(3-methyldimethoxysilyl)propyl]polypropylene oxide (O-Si) were purchased from Meryer CO., Ltd and used without further purification. 1 M LiPF_6 in ethylene carbonate (EC)/dimethyl carbonate (DMC) was kindly provided by Guangzhou Tinci Materials Technology Co., Ltd.

Preparation of NCM811 cathode. NCM811 powder was purchased from Guangdong Canrd New Energy Technology Co., Ltd. First, NCM811 powder, acetylene black (Li400), and poly(vinylidene fluoride) (PVDF, HSV900) with a weight ratio of 80:10:10 were mixed in N-methyl-2-pyrrolidone (NMP) using a Thinky mixer (AR-100). Then, the slurry was coated on an aluminum foil and dried under vacuum for 12 h. The active mass loading of NCM811 was controlled at about 3.0 mg cm^{-2} or 18 mg cm^{-2} (high loading).

Preparation of artificial F-Si layer, O-Si layer, and FO-Si layer. Taking artificial FO-Si@Li layer as a typical sample. Firstly, F-Si (0.5 mL) and O-Si (0.5 mL) were mixed in THF (1.0 mL) and deionized water (1.0 mL) with ammonia (0.2 mL) under stirring for 10 min. Then, the mixed solution was poured into a polytetrafluoroethylene (PTFE) dish and sealed at 60°C for 48 h. After further dried at 100°C under vacuum for 24 h, a FO-Si@Li layer was peeled off. For F-Si or O-Si layer, F-Si (1.0 mL) or O-Si (1.0 mL) was adopted, respectively.

Preparation of LMA with artificial SEI. Taking FO-Si@Li as a typical sample, Li foil was firstly immersed into the mixed solution of F-Si and O-Si (1:1 in volume) in tetrahydrofuran (THF) and standing for 1 h. After the reaction was over, the extra solution on the surface of Li foil was wiped with dust-free paper, denoted as FO-Si@Li. All procedure was executed inside an argon-filled glove box. F-Si@Li or O-Si@Li was prepared by immersing the Li foil in sole F-Si or O-Si THF solution, respectively.

Material characterization. The XRD measurement was conducted by a Bruker D8 Advance diffractometer at 40 kV and 40 mA with a Cu target tube and a graphite monochromator. The Li foil was sealing with Kapton tape during XRD measurement. The structural and morphological analysis were conducted using a scanning electron microscopy (TESCAN Brno, s.r.o. MAIA3) and X-ray photoelectron spectrometry (PerkinElmer PHI 1600 ESCA). The time-of-flight secondary-ion mass spectrometry (TOF-SIMS) was conducted on an TOF.SIMS5-100, and data of negative polarities were collected with Bi^+ at 25 kV as the ion source. AFM was carried out on a Bruker Dimension Fastscan microscope. The mechanical properties of samples were evaluated using a universal testing machine (Labthink XLW(PC)). In operando observation of Li deposition was conducted by an optical microscope camera with an in-situ cell (YM710TR).

Electrochemical measurements. NCM811 cathode was prepared by mixing NCM811 with acetylene black and polyvinylidene difluoride in N-methyl-2-pyrrolidone at a weight ratio of 80:10:10 using a Thinky (AR-100) mixer, resulting in a homogeneous slurry. Then, the slurry was coated on an aluminum foil and dried in a vacuum at 100°C over 24 h. The active cathode mass loading was 3 mg cm^{-2} , except for those high cathode mass loading of 18 mg cm^{-2} mentioned in this study. All electrochemical measurements were investigated by CR2032-type coin cells at room temperature, except for the pouch cell demonstrated in this study. A single-layer pouch cell was also assembled with a thin Li of $50 \mu\text{m}$. The electrolyte used in this study is 1 M LiPF_6 EC/DMC carbonate electrolyte, unless otherwise mentioned. The Li^+ transference number (t_{Li^+}) was measured according to the AC impedance (the frequency ranging from 10^6 Hz to 0.01 Hz) and direct-current (DC) polarization with a polarization voltage of 10 mV in Li||Li symmetric cell using a Potentiostat (VMP3, Bio-Logic). The t_{Li^+} was calculated according to the following Eq. (1)

$$t_{\text{Li}^+} = \frac{I_s(\Delta V - I_0 R_0)}{I_0(\Delta V - I_s R_s)} \quad (1)$$

in which ΔV is the polarization voltage, I_0 and I_s are the current before and after polarization, respectively, and R_0 and R_s are the charge-transfer resistance before and after polarization, respectively. Plating/stripping of Li||Li symmetric cells and galvanostatic charge-discharge test of Li||NCM811 full cells (cutoff voltage range of 3.0–4.3 V, $1 \text{ C} = 200 \text{ mAh g}^{-1}$) were carried out using a LAND CT2001A system. The energy density of full cell was calculated by (total capacity \times average voltage/total weight of cathode and anode).

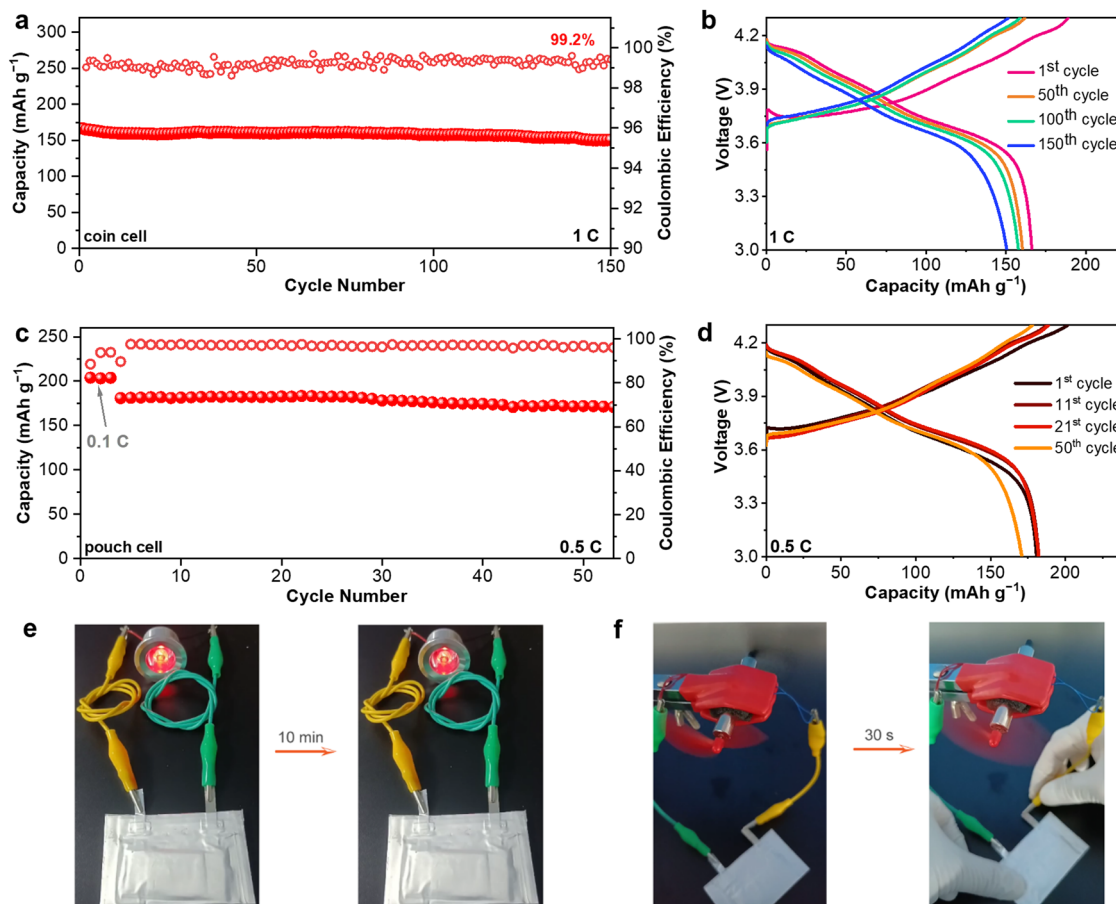


Fig. 7 Electrochemical performance of FO-Si@Li||NCM811 coin and pouch cells with a thin Li foil of 50 μm . **a** Cyclic performance and **b** selected GCD curves of FO-Si@Li||NCM811 coin cell at 1 C. **c** Cyclic performance and **d** selected GCD curves of FO-Si@Li||NCM811 pouch cell at 0.5 C. Optical photographs of the pouch cell **e** lighting up LEDs and **f** powering two micromotors.

Computational methods. All calculations were performed using the Gaussian 16 package, in which the specific structures were fully optimized by the B3LYP method with the basis set of 6-311++G (d, p). The binding energy (E_B) between artificial SEI (including FO-Si, F-Si or O-Si) and Li^+ is defined by Eq. (2) as following:

$$E_B = E_{\text{Li}^+ - \text{SEI}} - (E_{\text{Li}^+} + E_{\text{SEI}}) \quad (2)$$

Data availability

The data that support the findings of this study are available from the corresponding author upon request.

Received: 4 October 2022; Accepted: 6 February 2023;

Published online: 22 February 2023

References

- Dunn, B., Kamath, H. & Tarascon, J. M. Electrical energy storage for the grid: a battery of choices. *Science* **334**, 928–935 (2011).
- Goodenough, J. B. & Park, K. S. The Li-ion rechargeable battery: a perspective. *J. Am. Chem. Soc.* **135**, 1167–1176 (2013).
- Shi, F. et al. Lithium metal stripping beneath the solid electrolyte interphase. *Proc. Natl. Acad. Sci. USA* **115**, 8529–8534 (2018).
- Lin, D., Liu, Y. & Cui, Y. Reviving the lithium metal anode for high-energy batteries. *Nat. Nanotechnol.* **12**, 194–206 (2017).
- Duffner, F. et al. Post-lithium-ion battery cell production and its compatibility with lithium-ion cell production infrastructure. *Nat. Energy* **6**, 123–134 (2021).
- Bruce, P. G., Freunberger, S. A., Hardwick, L. J. & Tarascon, J. M. Li-O₂ and Li-S batteries with high energy storage. *Nat. Mater.* **11**, 19–29 (2011).
- Chen, P. Y. et al. Selective permeable lithium-ion channels on lithium metal for practical lithium-sulfur pouch cells. *Angew. Chem. Int. Ed.* **60**, 18031–18036 (2021).
- Zhang, X. Q. et al. A sustainable solid electrolyte interphase for high-energy-density lithium metal batteries under practical conditions. *Angew. Chem. Int. Ed.* **59**, 3252–3257 (2020).
- Li, L. et al. Self-heating-induced healing of lithium dendrites. *Science* **359**, 1513–1516 (2018).
- Yu, Z., Cui, Y. & Bao, Z. Design principles of artificial solid electrolyte interphases for lithium-metal anodes. *Cell Rep. Phys. Sci.* **1**, 100119 (2020).
- Meng, J. et al. Lithium ion repulsion-enrichment synergism induced by core-shell ionic complexes to enable high-loading lithium metal batteries. *Angew. Chem. Int. Ed.* **60**, 23256–23266 (2021).
- Wu, Q. et al. Dynamical SEI reinforced by open-architecture MOF film with stereoscopic lithiophilic sites for high-performance lithium-metal batteries. *Adv. Funct. Mater.* **31**, 2101034 (2021).
- Tikekar, M. D., Choudhury, S., Tu, Z. Y. & Archer, L. A. Design principles for electrolytes and interfaces for stable lithium-metal batteries. *Nat. Energy* **1**, 1–7 (2016).
- Albertus, P., Babinec, S., Litzelman, S. & Newman, A. Status and challenges in enabling the lithium metal electrode for high-energy and low-cost rechargeable batteries. *Nat. Energy* **3**, 16–21 (2017).
- Huang, M., Yao, Z., Yang, Q. & Li, C. Consecutive nucleation and confinement modulation towards Li plating in seeded capsules for durable Li-metal batteries. *Angew. Chem. Int. Ed.* **60**, 14040–14050 (2021).
- Yang, Q. et al. Ultrathin defective C–N coating to enable nanostructured Li plating for Li metal batteries. *ACS Nano* **14**, 1866–1878 (2020).
- Trinh, N. D. et al. An artificial lithium protective layer that enables the use of acetonitrile-based electrolytes in lithium metal batteries. *Angew. Chem. Int. Ed.* **57**, 5072–5075 (2018).
- Wang, H. et al. Dual-solvent Li-ion solvation enables high-performance Li-metal batteries. *Adv. Mater.* **33**, 2008619 (2021).

19. Amanchukwu, C. V. et al. A new class of ionically conducting fluorinated ether electrolytes with high electrochemical stability. *J. Am. Chem. Soc.* **142**, 7393–7403 (2020).
20. Chen, Y., Gong, Z. & Yang, Y. Enhanced electrochemical performance of high-energy lithium-sulfur batteries using an electrolyte with 1,1,2,2-tetrafluoro-3-(1,1,2,2-tetrafluoroethoxy)propane. *J. Electrochem. Soc.* **165**, A1915–A1919 (2018).
21. Shin, W. et al. Fluorinated co-solvent promises Li-S batteries under lean-electrolyte conditions. *Mater. Today* **40**, 63–71 (2020).
22. Fan, X. et al. All-temperature batteries enabled by fluorinated electrolytes with non-polar solvents. *Nat. Energy* **4**, 882–890 (2019).
23. Yu, Z. et al. Molecular design for electrolyte solvents enabling energy-dense and long-cycling lithium metal batteries. *Nat. Energy* **5**, 526–533 (2020).
24. Liu, F. et al. Fabrication of hybrid silicate coatings by a simple vapor deposition method for lithium metal anodes. *Adv. Energy Mater.* **8**, 1701744 (2018).
25. Chen, W. et al. Laser-induced silicon oxide for anode-free lithium metal batteries. *Adv. Mater.* **32**, 2002850 (2020).
26. Meng, J., Chu, F., Hu, J. & Li, C. Liquid polydimethylsiloxane grafting to enable dendrite-free Li plating for highly reversible Li-metal batteries. *Adv. Funct. Mater.* **29**, 1902220 (2019).
27. Wang, Y. et al. Lithium metal electrode with increased air stability and robust solid electrolyte interphase realized by silane coupling agent modification. *Adv. Mater.* **33**, 2008133 (2021).
28. Jiang, R. et al. An acetamide additive stabilizing ultra-low concentration electrolyte for long-cycling and high-rate sodium metal battery. *Energy Storage Mater.* **42**, 370–379 (2021).
29. Pathak, R. et al. Ultrathin bilayer of graphite/SiO₂ as solid interface for reviving Li metal anode. *Adv. Energy Mater.* **9**, 1901486 (2019).
30. Liu, W. et al. Core-shell nanoparticle coating as an interfacial layer for dendrite-free lithium metal anodes. *ACS Cent. Sci.* **3**, 135–140 (2017).
31. Wu, C. et al. Mesoporous silica reinforced hybrid polymer artificial layer for high-energy and long-cycling lithium metal batteries. *ACS Energy Lett.* **5**, 1644–1652 (2020).
32. Zhang, Q. et al. A multifunctional silicon-doped polyether network for double stable interfaces in quasi-solid-state lithium metal batteries. *Small* **18**, 2106395 (2022).
33. Luo, D. et al. Constructing multifunctional solid electrolyte interface via in-situ polymerization for dendrite-free and low N/P ratio lithium metal batteries. *Nat. Commun.* **12**, 186 (2021).
34. Wang, Q. et al. Rigid and flexible SEI layer formed over a cross-linked polymer for enhanced ultrathin Li metal anode performance. *Adv. Energy Mater.* **12**, 2103972 (2022).
35. Ma, Y. et al. A “blockchain” synergy in conductive polymer-filled metal-organic frameworks for dendrite-free Li plating/stripping with high coulombic efficiency. *Angew. Chem. Int. Ed.* **61**, 202116291 (2022).
36. Shi, Y. et al. A highly durable rubber-derived lithium-conducting elastomer for lithium metal batteries. *Adv. Sci.* **9**, 2200553 (2022).
37. Wu, W. et al. Safe and stable lithium metal batteries enabled by an amide-based electrolyte. *Nano-Micro Lett.* **14**, 44 (2022).
38. Zhang, D. et al. In situ construction a stable protective layer in polymer electrolyte for ultralong lifespan solid-state lithium metal batteries. *Adv. Sci.* **9**, 2104277 (2022).
39. Zhao, J. et al. Surface fluorination of reactive battery anode materials for enhanced stability. *J. Am. Chem. Soc.* **139**, 11550–11558 (2017).
40. Lin, D. et al. Conformal lithium fluoride protection layer on three-dimensional lithium by nonhazardous gaseous reagent freon. *Nano Lett.* **17**, 3731–3737 (2017).
41. Wu, D. X. et al. Li₂CO₃/LiF-rich heterostructured solid electrolyte interphase with superior lithiophilic and Li⁺-transferred characteristics via adjusting electrolyte additives. *Adv. Energy Mater.* **12**, 2200337 (2022).
42. Hu, J., Chen, K. & Li, C. Nanostructured Li-rich fluoride coated by ionic liquid as high ion-conductivity solid electrolyte additive to suppress dendrite growth at Li metal anode. *ACS Appl. Mater. Interfaces* **10**, 34322–34331 (2018).
43. Yang, Q., Hu, J., Meng, J. & Li, C. C–F-rich oil drop as a non-expendable fluid interface modifier with low surface energy to stabilize a Li metal anode. *Energy Environ. Sci.* **14**, 3621–3631 (2021).
44. Li, S. et al. A robust all-organic protective layer towards ultrahigh-rate and large-capacity Li metal anodes. *Nat. Nanotechnol.* **17**, 613–621 (2022).
45. Liu, Q. et al. Dendrite-free and long-cycling lithium metal battery enabled by ultrathin, 2D shield-defensive, and single lithium-ion conducting polymeric membrane. *Adv. Mater.* **34**, 2108437 (2022).
46. Betz, J. et al. Theoretical versus practical energy: A plea for more transparency in the energy calculation of different rechargeable battery systems. *Adv. Energy Mater.* **9**, 1803170 (2018).

Acknowledgements

This work was supported by the projects of National Natural Science Foundation of China (Nos. 22208118, 22005108), Natural Science Foundation of Guangdong Province (Nos. 2019B1515120027, 2021A1515110655, 2022B1515020005), China Postdoctoral Science Foundation (2021M691090), and Department of Science and Technology of Guangdong Province (Nos. 2021A0505030063, 2020B0101030005).

Author contributions

Q.Z. and Y.C. conceived and directed the project. L.C. and Q.Z. proposed the concept and designed the experiments. L.C. carried out the most experiments and analyzed the data. J.L. performed the electrochemical impedance measurements, Z.L. performed the computational study. H.Z. collected the XPS spectra. J.Y., and K.D. performed the in operando observation of Li deposition. L.C. wrote the manuscript, Q.Z. and Y.C. edited the manuscript. All authors contributed to the discussion.

Competing interests

The authors declare no competing interests.

Additional information

Supplementary information The online version contains supplementary material available at <https://doi.org/10.1038/s43246-023-00343-w>.

Correspondence and requests for materials should be addressed to Yue-Peng Cai or Qifeng Zheng.

Peer review information *Communications Materials* thanks Hongfa Xiang and the other, anonymous, reviewer(s) for their contribution to the peer review of this work. Primary Handling Editors: Jet-Sing Lee and Aldo Isidori.

Reprints and permission information is available at <http://www.nature.com/reprints>

Publisher's note Springer Nature remains neutral with regard to jurisdictional claims in published maps and institutional affiliations.



Open Access This article is licensed under a Creative Commons Attribution 4.0 International License, which permits use, sharing, adaptation, distribution and reproduction in any medium or format, as long as you give appropriate credit to the original author(s) and the source, provide a link to the Creative Commons license, and indicate if changes were made. The images or other third party material in this article are included in the article's Creative Commons license, unless indicated otherwise in a credit line to the material. If material is not included in the article's Creative Commons license and your intended use is not permitted by statutory regulation or exceeds the permitted use, you will need to obtain permission directly from the copyright holder. To view a copy of this license, visit <http://creativecommons.org/licenses/by/4.0/>.

© The Author(s) 2023